Materials Today Communications 40 (2024) 109597

Contents lists available at ScienceDirect

Materials Today Communications

journal homepage: www.elsevier.com/locate/mtcomm

Microstructure and hardness of $CoNiCrFeTi_x$ high-entropy alloy coatings prepared by laser cladding: Combining experimental and molecular dynamics simulation

Lu Xie [a,*], Guangda Wu [a,b], Xuefei Fu [c], Xinyang Wang [d], Chunyang Li [h], Qing Peng [f,g], Wenrui Wang [a,*], Yong Zhang [e], Yanbin Huang [d]

[a] School of Mechanical Engineering, University of Science and Technology Beijing, Beijing 100083, China
[b] Aero Engine Corporation of China, Beijing 102200, China
[c] Huai Hai Industrial Group CO., LTD, Shanxi Province, China
[d] Equipment Support and Remanufacturing Department, Army Academy of Armored Forces, Beijing 100072, China
[e] Beijing Advanced Innovation Center of Materials Genome Engineering, State Key Laboratory for Advanced Metals and Materials, University of Science and Technology Beijing, Beijing 100083, China
[f] State Key Laboratory of Nonlinear Mechanics, Institute of Mechanics, Chinese Academy of Sciences, Beijing 100190, China
[g] School of Engineering Sciences, University of Chinese Academy of Sciences, Beijing 100049, China
[h] China Aerospace Science & Industry Corp., Inner Mongolia, China

ARTICLE INFO

Keywords:
Laser cladding
High-entropy alloy
Molecular dynamics
Microhardness
Nanoindentation

ABSTRACT

Laser cladding technology offers several advantages over alternative coating methods, including rapid cooling, low dilution rate, and effective metallurgical bonding between the coating and matrix. However, there is limited understanding regarding the microstructures and properties of laser-cladded high-entropy alloy (HEA) coatings. Thus, our research aims to investigate the characteristics and performance of $CoNiCrFeTi_x$ (x = 0.1, 0.3, 0.5, 0.7) HEA coatings, produced through laser cladding, on Q235 steel substrates We employ molecular dynamics (MD) simulation and experimental techniques to examine the impact of Ti element content on the structure and hardness of the cladding layer. The MD simulation accurately reproduces the melting and nucleation processes of crystal structures, providing insights beyond what is observable through experiments alone. Our results reveal that the cladding layer is predominantly composed of an FCC phase, with an increasing presence of a BCC phase as the Ti content rises. Correspondingly, experimental observations confirm that the $CoNiCrFeTi_x$ HEA coating primarily consists of the FCC phase, while FeCr, Ni_2Ti, and Co_2Ti phases emerge with higher Ti content.The cladding layer exhibits a characteristic dendritic (DR) structure, where the interdendritic (ID) region expands as Ti content increases. Additionally, we conducted surface hardness testing on the cladding layer. The hardness of the cladding layer increases with the increase of Ti content, and the increase in Ti content enhances the stability of the dislocation density in the cladding layer.

1. Introduction

Coatings play a crucial role in enhancing properties, such as hardness, corrosion-resistance, and wear resistance, making them widely applicable in demanding fields such as aviation, military, electric power, and shipbuilding [1,2]. High-entropy alloys, characterized by exceptional attributes such as high strength, hardness, radiation resistance, oxidation resistance, and wear resistance, show promise as potential materials for high-performance coatings [3,4].

Among various coating preparation technologies, laser cladding technology stands out due to its advantageous features of rapid cooling, low dilution rate, and the ability to achieve a metallurgical bond between the coating and substrate. Laser cladding has been extensively employed to fabricate HEA coatings on a macroscopic scale. For instance, Shu et al. [5] investigated the microstructure and high-temperature wear mechanism of laser-cladded CoCrNiSiBFe HEA amorphous coatings. They observed a substantial improvement in wear resistance due to the high hardness of the amorphous phase. Huang et al.

* Corresponding authors.
E-mail addresses: xielu@ustb.edu.cn (L. Xie), gmbitwrw@ustb.edu.cn (W. Wang).

https://doi.org/10.1016/j.mtcomm.2024.109597
Received 20 March 2024; Received in revised form 15 June 2024; Accepted 17 June 2024
Available online 19 June 2024

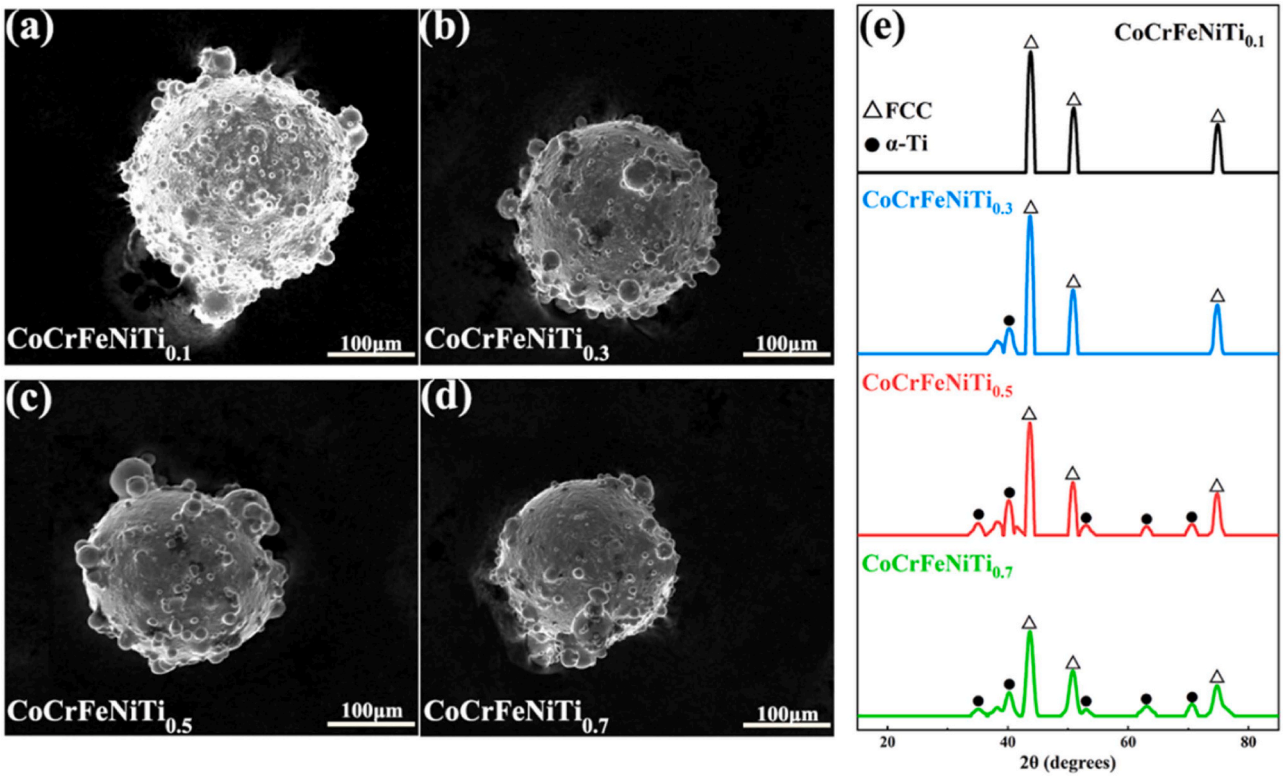

Fig. 1. SEM images (a-d) and XRD (e) scanning results of CoNiCrFeTi$_x$ (x=0.1, 0.3, 0.5, 0.7) HEA powder particles.

[6] successfully produced TiVCrAlSi HEA coatings, which exhibited finer grain sizes, enhanced hardness, and improved wear resistance. Ye et al. [7] accomplished the preparation of CrMnFeCoNi HEA coatings on 304 stainless steel substrates and demonstrated excellent corrosion resistance, along with a preliminary exploration of the coating's mechanical properties. Zhang et al. [8] developed AlCoCrFe$_x$Ni (x = 1.5, 2.5) HEA coatings, revealing the presence of disordered BCC (A2) phase enriched with Fe-Cr and ordered BCC (B2) phase enriched with Al-Ni. The AlCoCrFe$_{2.5}$Ni coating exhibited enhanced strength and wear resistance attributed to the strengthening effect of B2 precipitates. Qiu et al. [9] manufactured Al$_2$CrFeNiCoCuTi$_x$ HEA coatings and investigated the influence of Ti content on the coating. Driven by the high-entropy effect, this coating exhibited a tendency to form FCC, BCC, and Laves phases, with BCC phases increasing with higher Ti content. Furthermore, the wear resistance of the Al$_2$CrFeNiCoCuTi$_x$ coating was significantly improved. Exploiting the affinity between Ti and N, Guo et al. [10] prepared CoCr$_2$FeNiTix HEA coatings in an air atmosphere, observing the presence of nanoscale TiN reinforced particles that notably enhanced the wear resistance of the coating.

MD simulation is a well-established approach for investigating the atomic-level behaviors, kinetics, and properties of materials [10]. It allows for direct observation of microstructural changes and evolution within a short time frame [11,12], making it a valuable complement to traditional experiments and theoretical analyses [13–22]. Numerous researchers have employed MD simulations to investigate laser processing phenomena. For example, Li et al. [23] conducted MD simulations to examine the mechanical properties of AlCrFeCuNi HEA under uniaxial tensile loading, revealing lattice distortion, dislocation slip, and twinning during the plastic deformation process. Zhang et al. [24] employed MD simulations to investigate the laser selective melting process of $Zr_{90}Cu_{10}$ alloy, exploring the crystallization behavior of amorphous alloys during laser melting. They discovered that the laser scanning speed significantly influences the crystallization level, with a notable increase in BCC content at lower speeds while higher speeds suppress crystallization nucleation. Kurian et al. [25] utilized MD simulations to study the nucleation and growth process of aluminum nanoparticles within the molten pool during SLM. By directly controlling the temperature of the molten pool, they simulated the local heating and rapid solidification process, elucidating that the cooling rate within the molten pool governs the uniform nucleation of equiaxed crystals at the center of the molten pool. Chen et al. [26] employed MD simulations to investigate the atomic crystallization and microstructure evolution of FeCrNi medium-entropy alloy during the SLM process. They observed a significant presence of stacking faults (SFs) at the molten pool boundaries and the segregation of nano-scale chromium-rich clusters. Adjusting the laser power and scanning speed offered potential mitigation strategies for the observed segregation phenomena. Despite the extensive application of MD simulations in coating research, the microstructure evolution and properties of CoNiCrFeTi$_x$ processed through laser cladding remain elusive.

This investigation examined the microstructure and evolution of CoNiCrFeTi$_x$ (x = 0.1, 0.3, 0.5, 0.7) HEA coatings fabricated through laser cladding. A combination of experimental techniques and MD simulations was employed to gain comprehensive insights. Furthermore, the strengthening effects of the CoNiCrFeTi$_x$ (x = 0.1, 0.3, 0.5, 0.7) cladding layer were analyzed.

2. Methods

2.1. Experimental materials and methods

In this investigation, CoNiCrFe HEA powder was synthesized using the vacuum melting atomization method, employing Co, Cr, Fe, and Ni metal blocks. Additionally, Ti powder was produced through planetary grinding, Ti powder of different contents was mixed into CoNiCrFe, using the ND-L planetary ball mill with stainless steel grinding balls. The ball-to-powder ratio was 10:1, the ball milling time was 2 hours, and the ball milling speed was 350 r/min. Subsequently, CoNiCrFeTi$_x$ (x = 0.1, 0.3, 0.5, 0.7) HEA powder is formed. In Fig. 1(a-d), as the Ti powder content continues to increase, the obtained powder particles gradually

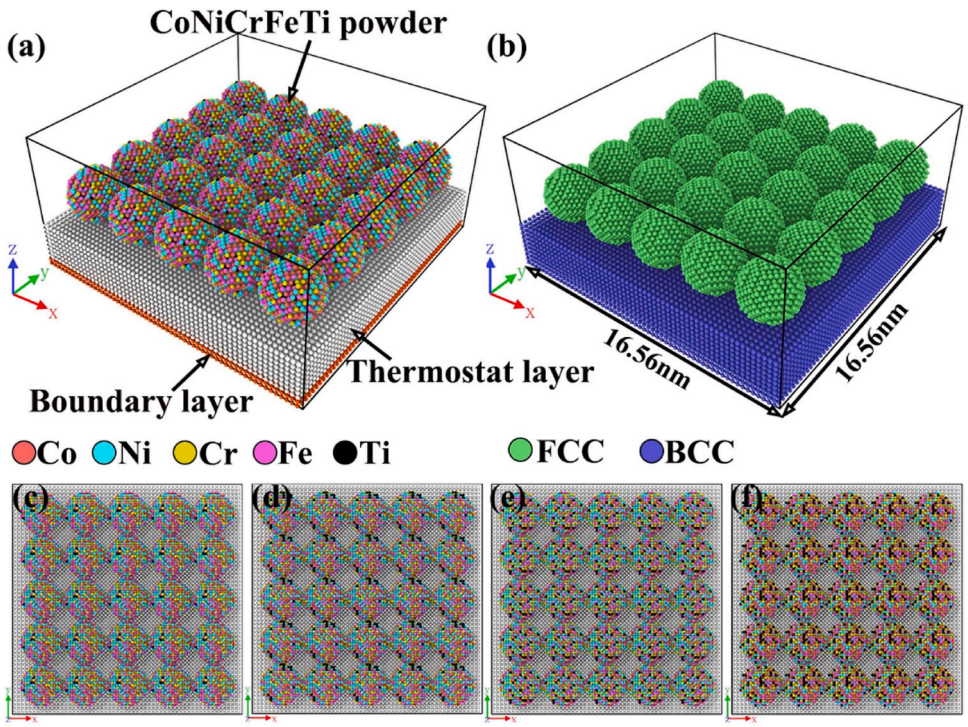

Fig. 2. Models of CoNiCrFeTi$_x$ HEA powder particles. 3D View (a), and Phase Structure Diagram (b), Ti Element Content (x = 0.1, 0.3, 0.5, 0.7) (c)-(f).

decrease in size. The powder particles in the largest group have a diameter of around 230 μm, while the powder particles in the smallest group have a diameter of around 180 μm. This is attributed to the relatively large atomic radius of the Ti element and its significantly negative mixing enthalpy when combined with other constituent elements[27,28]. It readily forms lattice distortions, increasing the powder's brittleness and internal stresses, thereby promoting the deformation and fracture processes during ball milling. Therefore, the addition of Ti elements leads to a reduction in the size of powder particles. Fig. 1(e) shows the XRD results of the CoNiCrFeTi$_x$ powder, indicating that the powder particles are primarily composed of a FCC solid solution structure, along with characteristic peaks of a small amount of elemental Ti. The substrate utilized in the study consisted of Q235 steel, and 30 mm × 30 mm × 10 mm substrate samples were obtained via wire cutting. Before the laser cladding process, the surface of the substrate was cleaned. Firstly, the substrate surface was polished using 200#, 600#, …, 2000# sandpaper to remove the surface oxide layer. Then, the substrate was immersed in anhydrous alcohol and cleaned using an ultrasonic cleaner for 20 minutes to remove impurities and oil stains. Finally, the substrate was subjected to drying treatment.

The laser cladding equipment employed was an LDF3000–60 high-power semiconductor laser integrated with an RX160 six-axis mid-load manipulator. The laser system operated at a rated working voltage of 380–480 V and an output power range of 0–10 kW. Specific parameters were selected for the laser cladding process, including a laser scanning speed of 4 mm/s, laser power of 1.2 kW, and an overlap rate of 30 %. The phase structure of the cladding layer was analyzed using a D8 X-ray diffractometer (XRD). The scanning range was set from 20° to 90° at a scanning speed of 2°/min, with a step size of 0.02°. Microstructural observations of the cladding layer were conducted using a Novan OSM 450/650 environmental scanning electron microscope (SEM), and the equipment is also equipped with a FeatureMax-type X-ray energy dispersive spectrometer (EDS). To measure the cross-section hardness of the cladding layer, a MICROMET-6030 Vickers microhardness tester was utilized. The loading force during the loading process is 0.49 N, and the loading time is 10 s. The hardness measurements were taken at intervals of 4 mm from the surface to the substrate, with each interval treated as a test column. Four tests were performed on each test column, and the average value was recorded.

2.2. MD simulations

The laser cladding model employed in this study consisted of CoNiCrFeTi$_x$ (x = 0.1, 0.3, 0.5, 0.7) powder and an Fe substrate. Fig. 2, illustrates the configuration, where the CoNiCrFeTi$_x$ (x = 0.1, 0.3, 0.5, 0.7) powder layer consists of 25 particles, each with a diameter of 3 nm and a particle-to-particle distance of 3 Å. The initial crystal structure of CoNiCrFeTi$_x$ is face-centered cubic (FCC), with a lattice constant of 3.6147 Å. The substrate size is 16.56 nm × 16.56 nm × 2.57 nm. The substrate comprises two layers: the boundary layer and the thermostat layer. The boundary layer serves to prevent interference from reflected waves and non-physical effects during the simulation. Above the boundary layer, the thermostat layer replicates the constant temperature conditions typically encountered in experimental setups, facilitating better control over temperature gradients and heat conduction processes. The temperature of the thermostat layer is maintained at 300 K using the Langevin thermostat method. Atom motion within the thermostat layer adheres to Newton's second law of classical mechanics. The atomic interactions of Co-Cr-Fe-Ni were described using a many-body embedded-atom potential, widely employed in MD simulations of CoNiCrFe HEA [29–33]. Lennard-Jones potential and Lorenz-Berthelot mixing rules [34,35] were utilized to describe other atomic interactions involving Co, Cr, Fe, Ni, and Ti. Periodic boundary conditions were applied in the x and y directions, while aperiodic fixed boundary conditions were used in the z direction. The simulation utilized a time-step of 0.002 ps. The laser cladding simulation was divided into two stages: heating and cooling. Throughout the simulation, the micro-canonical ensemble (NVE) was employed.

The MD simulations were performed using the Large-scale Atomic/Molecular Massively Parallel Simulator (LAMMPS) [36]. In the heating process, the "fix heat" command in LAMMPS was utilized to simulate the laser beam's effect. This method involves adding non-translative kinetic energy to the atoms within the laser-affected region to simulate the laser heating process. The laser was uniformly scanned along the positive

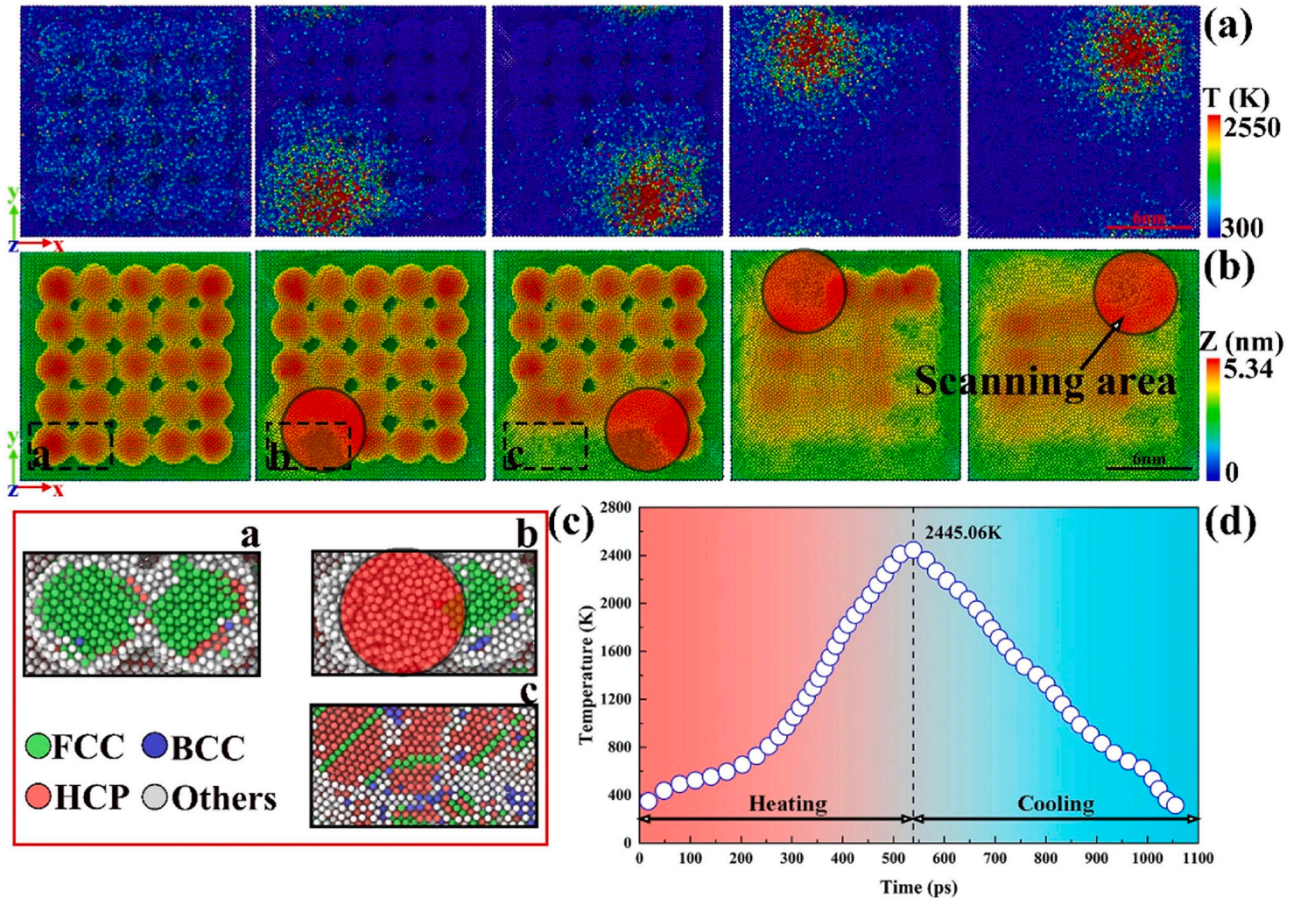

Fig. 3. Laser melting process. the distribution of atomic temperatures during the laser cladding process (a), the melting process of $CoNiCrFeTi_{0.1}$ HEA powder particles (b), the morphological changes of powder particles during laser heating (c), the morphology before heating (c-a), the morphology during heating (c-b), the morphology after cooling (c-c), and the temperature variation of powder particles at the moment of laser heating (d).

Y-axis at a speed of 0.1 nm/ps for 5 cycles. During the cooling process, the substrate temperature was maintained at approximately 300 K to facilitate the cooling of the cladding powder. The OVITO visualization software [37] was employed to analyze the atomic distribution and observe the microstructure evolution during laser cladding. The atomic microstructure was characterized using Common Neighbor Analysis (CNA) [38], and Radial Distribution Function (RDF) [39] patterns.

Following the completion of the laser cladding simulation, a nano-indentation simulation was conducted on the cladding layer. The compression process resulted in surface indentations on both the cladding layer and the substrate. The kinematic and dynamic information within the indentations was measured. The same potential function used in the laser cladding simulation was employed. A spherical virtual indenter with a radius of 2 nm applied a downward force along the Z-axis at a velocity of 10 m/s, resulting in an indentation depth of 3 nm. One of the advantages of MD simulations is the ability to access both the dynamic and kinematic information of atoms. During the virtual indentation process, the reaction forces (F) acting along the Z-axis were recorded at each position. Hardness (H), which characterizes a material's resistance to plastic deformation, was calculated using the formula $H = F_{max}/A$[40], where F_{max} represents the maximum applied load at that point and $A = \pi(2R\text{-}h)h$ (R is the indenter radius, h is the indentation depth) represents the projected area of the indentation at that point. Thus, the hardness at each position was determined. Further analysis is described in Section 3.3.

3. Results and discussion

3.1. Laser cladding process and crystal structure evolution

Fig. 3(a) and (b) respectively show the temperature distribution and height variation in the top view (Z direction) of the model during the laser cladding process. They also display the laser scanning path during the laser cladding of $CoNiCrFeTi_{0.1}$ powder particles, with the cladding process involving five back-and-forth laser scans along the X-direction. The surface morphology changes of the $CoNiCrFeTi_{0.1}$ powder particles during the laser scanning process are presented in Fig. 3(b), with atoms colored according to their height along the Z-direction. The red circular shaded area in Fig. 3(b) represents the region affected by the laser beam. Upon laser application, the powder particles begin to melt, resulting in a decrease in the average height within the region. Fig. 3(d) illustrates the temperature variation of two powder particles, as indicated by the dashed rectangle in Fig. 3(b), throughout the laser scanning process. Within a short period, the temperature within the region rapidly increases, reaching a peak of 2500 K, and subsequently decreases swiftly to approximately 300 K. This temperature behavior aligns with the high heating and cooling rates typically observed during laser processing. Fig. 3(a) color-codes the particle temperature, providing an overview of the temperature variation as the laser beam moves. The region exposed to the laser irradiation center exhibits higher temperatures, while the temperatures in the surrounding areas gradually decrease as they move away from the laser center until reaching room temperature. The distribution trend of temperature is related to the thermal motion of atoms.

To investigate the microscopic structural changes of $CoNiCrFeTi_{0.1}$

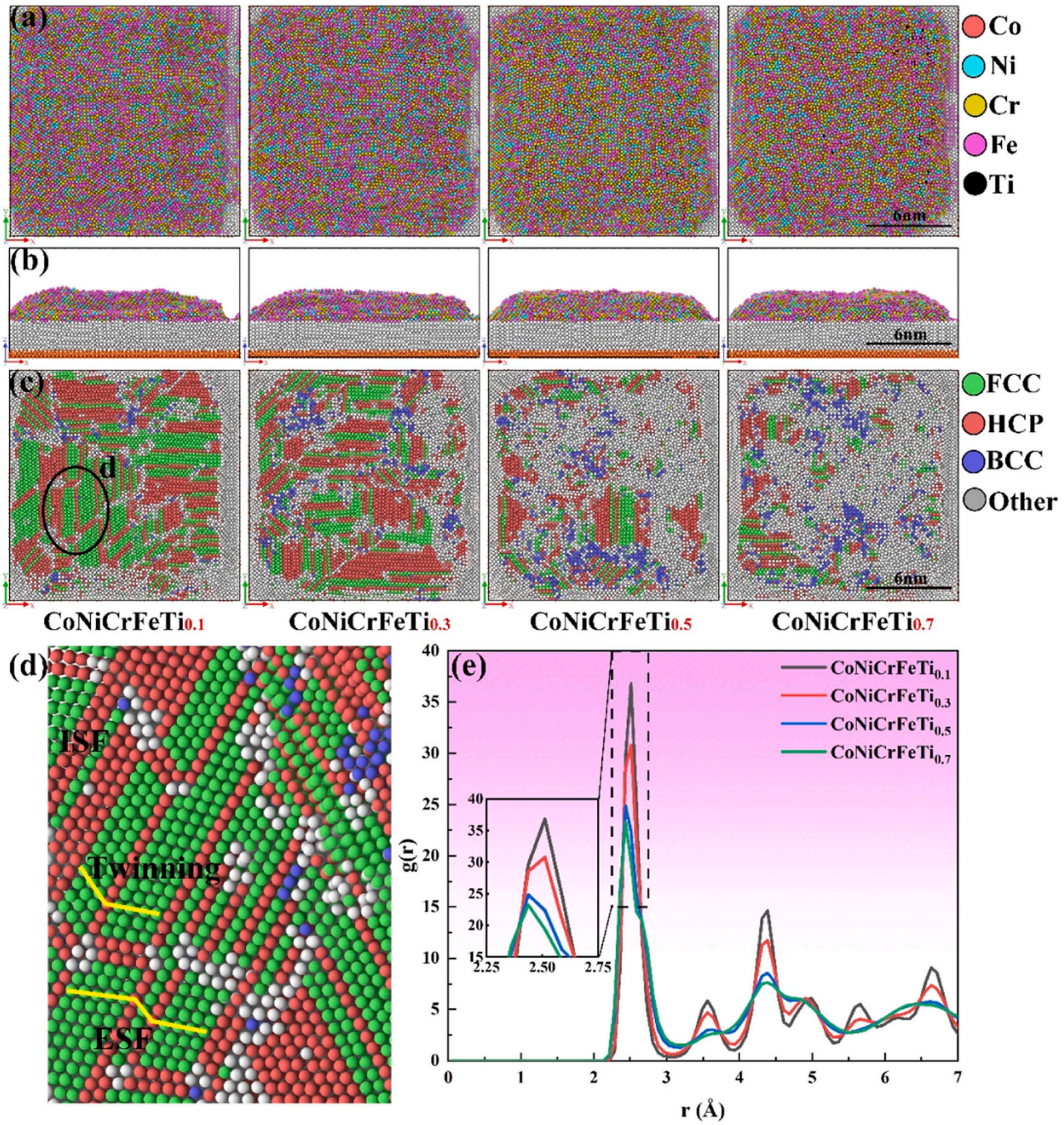

Fig. 4. Microstructure of $CoNiCrFeTi_x$ (x = 0.1, 0.3, 0.5, 0.7) HEA during the laser cladding process. Morphology and CNA of the cladding layer (a-c), formation of twinning and stacking fault during the cladding process (d), RDF curve of the cladding layer (e).

HEA powder during the laser cladding process, a common neighbor analysis (CNA) was performed on the particle models within the dashed rectangle in Fig. 3(b) as an example. This analysis enables the visualization of the evolution process of FCC, HCP, and BCC clusters. Fig. 3(c) illustrates the primary crystal structure changes during the heating process. Upon laser application, the crystal structure of these particles dissolves, transitioning into a disordered state. Subsequently, the molten powder undergoes cooling and solidification, as depicted in Fig. 3(d). Rapid cooling occurs as the molten HEA powder interacts with the substrate. Nucleation initiates within the solidification region along the laser scanning direction. Due to the high cooling rate, the nucleation process occurs almost instantaneously, with disordered atoms gradually transforming into crystalline structures characterized by FCC and HCP layers, accompanied by the presence of a small amount of BCC structure.

3.2. Morphology and phase structure analysis

Under the influence of a high-energy laser, $CoNiCrFeTi_x$ (x = 0.1, 0.3, 0.5, 0.7) HEA powders were melted and deposited onto the substrate surface, resulting in the formation of HEA coatings. Fig. 4(a-c) respectively illustrate the laser-cladded layers of $CoNiCrFeTi_x$ HEA with four different Ti contents. Fig. 4(a) and 4 (b) depict the elemental distribution in the top view (Z direction) and front view (Y direction) of the model after cladding, respectively. Fig. 4(c) displays the cross-sectional CNA analysis in the top view (Z direction), revealing the phase structure of the cladded layer. These cladding layers exhibit well-formed

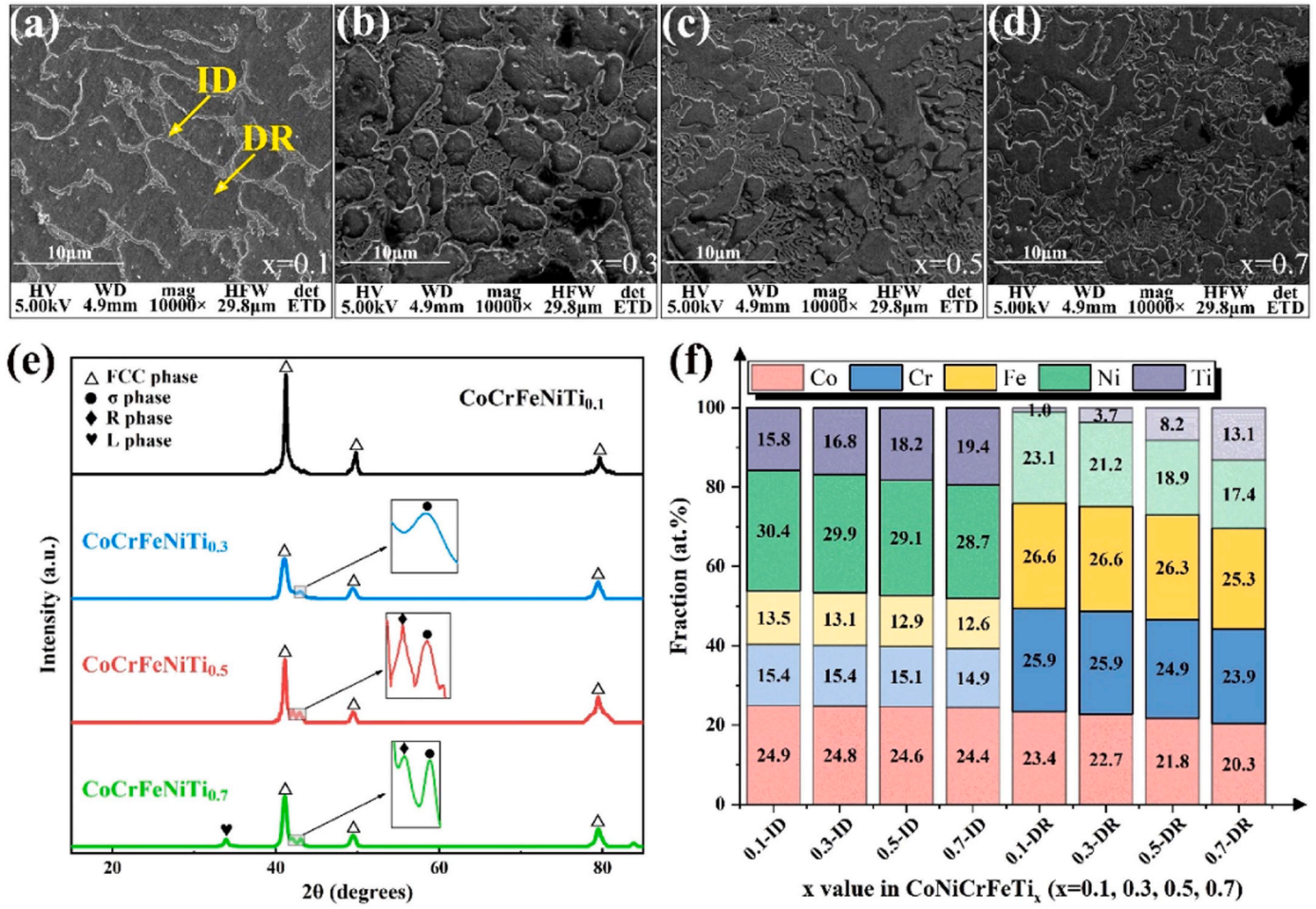

Fig. 5. SEM scanning results of CoNiCrFeTi$_x$ (x=0.1, 0.3, 0.5, 0.7) HEA cladding layers (a-d). Experimental XRD diffraction pattern (e). Distribution of elements in ID and DR regions of CoNiCrFeTix (x=0.1, 0.3, 0.5, 0.7) (f).

structures without apparent defects. Notably, the cladding layers display a characteristic pattern of lower height at the sides and higher height at the center. CNA was conducted on the four cladding layers, revealing their primary composition of FCC, HCP, and BCC phases. Moreover, Fig. 4(c-d) illustrates the formation of twinning, dislocations, and stacking faults (SFs). These observations can be attributed to varying heating levels in different regions, resulting in temperature gradients. During the heating process, lattice slip occurs in multiple directions, inducing residual stresses on the surface of the HEA cladding layers. This leads to the presence of internal stacking faults (ISF) and external stacking faults (ESF) in Fig. 4(d). SFs and twinning, as stable planar defects, effectively hinder dislocation motion; thus, enhancing the material's strength and toughness. In Fig. 4(c) and (e), for x = 0.5 and 0.7, there is an increase in the content of BCC and disordered atoms, accompanied by a significant decrease in FCC content. This transition indicates a shift in the cladding layer towards an amorphous phase structure. Fig. 4(e) presents the RDF analysis of the four cladding layers. RDF describes the distribution of neighboring particles surrounding a particular particle [41–43]. The shape of the peaks reflects the spatial ordering of atoms, with sharp peaks indicating ordered atomic arrangements and rounded peaks indicating disorder. This analysis enables the distinction between crystalline and amorphous structures [44].

All four cladding layers exhibit crystalline characteristics, displaying a series of relatively sharp peaks representing atomic arrangements. By examining the first peak, it is evident that with increasing Ti element content, the peak height significantly decreases and the peak width increases. This signifies a weakening of the crystalline characteristics, consistent with the CNA observations.

Fig. 5(a-d) presents the SEM micrographs of the CoNiCrFeTi$_x$ (x = 0.1, 0.3, 0.5, 0.7) HEA coatings. The microstructure of these coatings exhibits a typical dendritic morphology, where the interdendritic areas are represented by gray regions and the dendritic regions are indicated by black regions, as labeled in Fig. 5(a). When comparing the influence of Ti element content on the microstructure of the coatings, an increase in Ti content leads to a higher relative area of interdendritic regions. In Fig. 5(f), the distribution and segregation of elements in the cladding layer were analyzed using EDS. The content of Co and Ni elements in the interdendritic regions is significantly higher than that of Ti. In terms of elemental distribution, the interdendritic regions are primarily enriched with Ni and Co, while the dendritic cores are mainly enriched with Cr and Fe. Furthermore, as the Ti content increases, this segregation phenomenon is significantly alleviated. Fig. 5(e) displays the XRD patterns obtained from the experimental CoNiCrFeTi$_x$ (x = 0.1, 0.3, 0.5, 0.7) cladding layers. For each composition, three distinct sets of diffraction peaks appear around 40°, 50°, and 80°. The main phase of the cladding layers is a solid solution with an FCC structure. Notably, as the Ti element content increases, the positions of the FCC peaks shift towards smaller angles. This shift can be attributed to the relatively large atomic radius of Ti atoms, which readily incorporate into the FCC matrix, causing lattice distortions and increasing the interplanar spacing. Consequently, the corresponding diffraction angles of the matrix decrease. The lattice constant of the CoNiCrFeTix high-entropy alloy was calculated using the Bragg equation, which is expressed as follows:

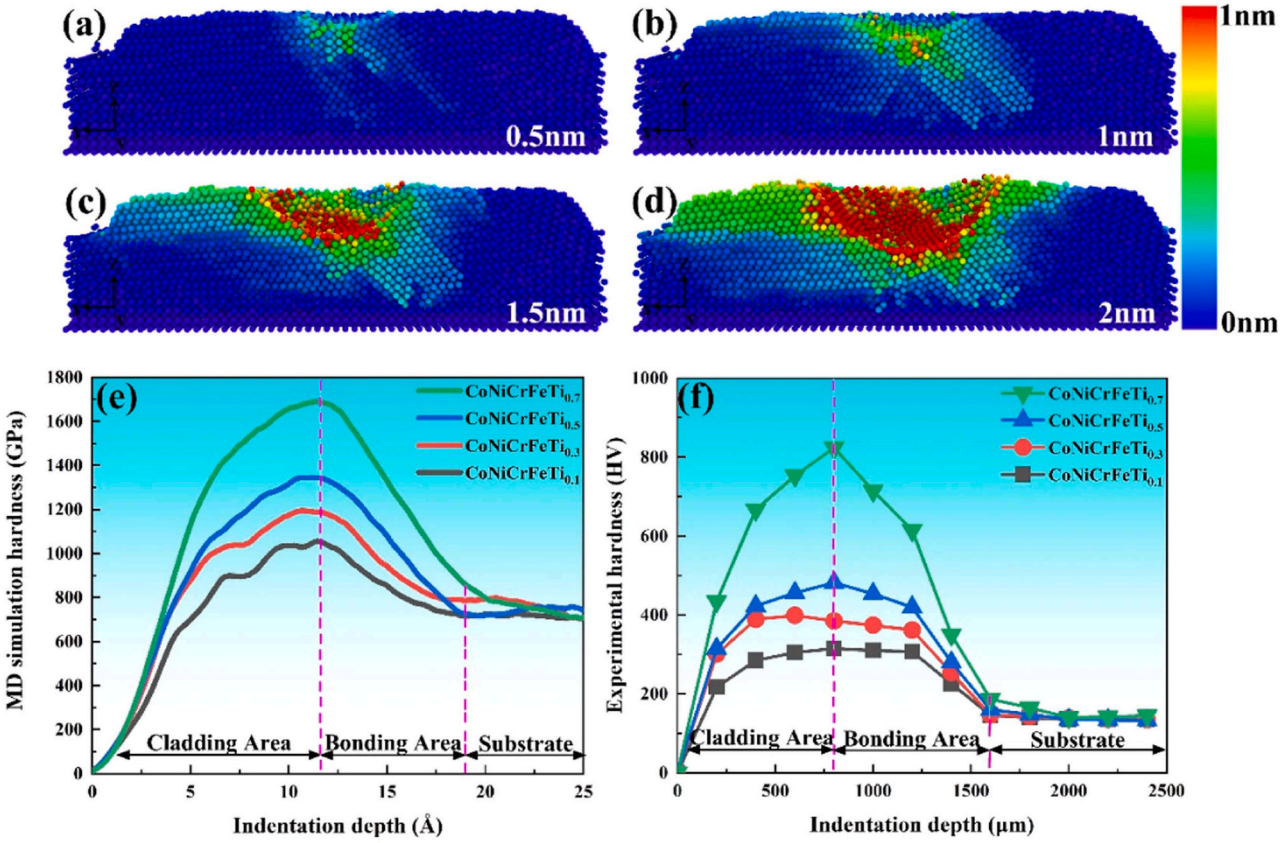

Fig. 6. Nanoindentation process of the CoNiCrFeTi$_x$ HEA cladding layer. Atomic displacement maps for indentation depths of 0.5 nm, 1 nm, 1.5 nm, and 2 nm are shown in (a)-(d), Nanohardness depth-hardness curves, simulated values (e) and experimental values (f).

$$a = \frac{\lambda}{2\sin\theta}\sqrt{H^2 + K^2 + L^2} \tag{1}$$

In the equation, λ is the diffraction wavelength, *HKL* is the diffraction plane index, and θ is the glancing angle. The calculation results indicate that the lattice constants of the CoNiCrFeTi$_x$ (x = 0.1, 0.3, 0.5, 0.7) HEA are 3.491 Å, 3.537 Å, 3.587 Å, and 3.613 Å, respectively. The larger atomic radius of Ti atoms tends to exacerbate the lattice distortion effect within the CoNiCrFe alloy, increasing the alloy lattice constant. Currently, the atomic radius difference δ is primarily used to characterize the severity of the lattice distortion effect in the alloy, and its expression is shown as follows [45]:

$$\delta = \sqrt{\sum_{i=1}^{N} c_i(1 - r_i/\bar{r})^2} \tag{2}$$

In the equation, r_i represents the atomic radius of constituent elements, $\bar{r}$ is the average atomic radius in the alloy, and c_i is the content of each constituent element. The calculation results indicate that the atomic radius differences of the CoNiCrFeTi$_x$ (x = 0.1, 0.3, 0.5, 0.7) HEA are 0.025, 0.040, 0.050, and 0.057, respectively. It can be observed that there is a significant positive correlation between the alloy lattice constant and the content of Ti elements and the atomic radius difference. Combining Fig. 5(f) and (e), an FeCr intermetallic compound (σ phase) appears in the cladded layer at x=0.3. At x=0.5, in addition to the σ phase, a precipitation of the Ni_2Ti (R phase) intermetallic compound is observed. At x=0.7, the presence of the Co_2Ti (L phase) is also observed.

3.3. Hardness

After completing the laser cladding, we performed nanoindentation on the surface of the CoNiCrFeTi$_x$ HEA cladding layer. The specific parameters for the indentation process are detailed in Section 2.2. To examine the atomic movement of the CoNiCrFeTi$_x$ HEA coating during nanoscale indentation, atoms were color-coded based on their displacement. Fig. 6(a-d) presents sequential atomic displacements in the alloy at varying indentation depths. During the indentation process, the shape of the indentation closely matches the shape of the indenter, forming a spherical indentation. At indentation depths of 1 nm and 1.5 nm, as shown in Fig. 6(b) and (c), the atomic displacements around the indenter markedly increase. Some atoms experience slip in the –45° and –135° directions, considering the negative direction of the x-axis as positive, and the plane of the layer surface where the x-axis resides. Fig. 6(e) and (f) respectively show the hardness-indentation depth curves obtained from MD simulation and experiments. The three regions on the horizontal axis correspond to the coating deposition zone (Cladding Area), the coating-substrate interface (Bonding Area), and the substrate material (Substrate). This curve first rises, then declines, and eventually stabilizes in Fig. 6(e). The pattern of the hardness-depth curves for various Ti concentrations is broadly consistent. Within the 0–12 Å indentation depth, there is a steady hardness increase. From 12 Å to 18 Å, the hardness swiftly diminishes, and post an 18 Å depth, it remains consistent. The increment in hardness from 0–12 Å is attributed to the coating area. Within this segment, the HEA coating is of superior quality, indicating advanced surface strengthening, which significantly improves the hardness. The pronounced decline in hardness from 12 Å to 18 Å is associated with the transition zone between the coating and the substrate. In this zone, the strengthening effect is muted, resulting in a hardness decrease. Past 18 Å, the stabilized hardness represents the substrate. Simulations underscore that the coating's hardness surpasses that of the substrate.

Applying a CoNiCrFeTi$_x$ HEA coating to a substrate not only augments its surface strength but also offers protection. Additionally, as the

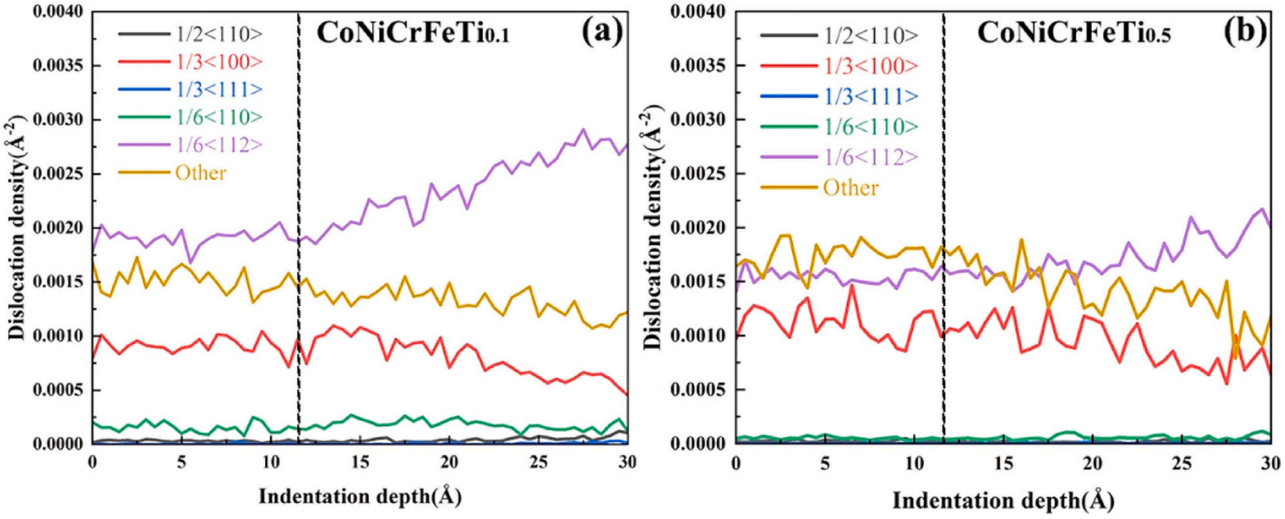

Fig. 7. Variation of dislocation density during nanoindentation process.

Ti element content rises, there is a corresponding uptick in the coating's hardness. A peak hardness value is observed at x = 0.7, registering at 1690.0 GPa. This is 1.60 times greater than the hardness recorded at x = 0.1. Fig. 6(f) illustrates the relationship between hardness and depth for $CoNiCrFeTi_x$ (with x = 0.1, 0.3, 0.5, 0.7) HEA coatings, as determined experimentally. These empirical hardness-depth curves for varying HEA coatings align with trends seen in MD simulations. Hardness readings remain elevated within the 0–1200 μm range from the coating surface, peaking between 400–800 μm. Nonetheless, post 1200 μm, there is a sharp decline in hardness. After 1600 μm, the hardness measures across the various compositions tend to converge and subsequently level off. The maximum hardness is marked at x = 0.7, achieving 830.3 HV, which stands at 2.13 times the hardness seen at x = 0.1.

There exists a discrepancy between experimental and computational findings, predominantly stemming from variations in simulation conditions and experimental configurations. While MD simulations operate at the nanoscale where size effects are paramount, the hardness values derived from both simulations and experiments align in magnitude and display comparable trends. Thus, utilizing MD simulations to delve into the nuances of the nanoindentation process is justified.

Fig. 7 presents the variation of dislocation density within $CoNiCrFeTi_x$ HEA during nanoindentation process. The dislocation density is more stable in $CoNiCrFeTi_{0.5}$ HEA during nanoindentation, while the variation of dislocations within $CoNiCrFeTi_{0.1}$ HEA is relatively larger, especially in terms of Shockley dislocations [46–49]. Within the $CoNiCrFeTi_x$ HEA, the integration of Ti atoms amplifies lattice distortion, which in turn bolsters resistance to dislocation movement and hinders slip, which also results in $CoNiCrFeTi_{0.5}$ having a higher hardness than $CoNiCrFeTi_{0.1}$. In Fig. 7(a), the strength of $CoNiCrFeTi_{0.1}$ reaches its maximum near the black dashed line (Fig. 6e). Before the black dashed line, the dislocation density remains relatively stable, while significant changes occur afterward, indicating pronounced dislocation slip. This also leads to a decrease in strength during the indentation process (Fig. 6e). Simultaneously, with the increase of Ti content, the emergence of the σ phase (Fig. 5), characterized by rigid intermetallic compounds, results in constrained slip systems and elevated hardness. The crystallization of these robust phases boosts the alloy resilience against elastic and plastic deformation, as well as fracture. These precipitates, distributed uniformly within the matrix, play a pivotal role in precipitation strengthening, thereby enhancing the overall alloy strength and hardness.

4. Conclusions

We undertook a detailed examination of the microstructure and attributes of $CoNiCrFeTi_x$ (x = 0.1, 0.3, 0.5, 0.7) HEA coatings produced via laser cladding. This was achieved through a synergistic approach, integrating experimental procedures with MD simulations. Throughout the MD simulations, the FCC, HCP, and BCC configurations emerged progressively during the cooling phase, with the FCC configuration emerging as the dominant phase. The $CoNiCrFeTi_x$ HEA layers, as synthesized experimentally, were predominantly characterized by the FCC phase. With an uptick in Ti content, other phases, such as FeCr, Ni_2Ti, and Co_2Ti, manifested. A rise in the Ti content augmented the ID area, and the secondary dendrite arms evolved to be more refined. Simultaneously, the hardness of the cladding layer gradually increased. MD simulations indicated that the increase in hardness of the cladding layer is associated with its ability to maintain a relatively stable dislocation density.

CRediT authorship contribution statement

Chunyang Li: Writing – original draft, Validation, Investigation. **Qing Peng:** Software, Project administration, Funding acquisition. **Wenrui Wang:** Supervision, Project administration, Methodology, Funding acquisition. **Yong Zhang:** Resources, Project administration, Conceptualization. **Yanbin Huang:** Resources, Project administration. **Lu Xie:** Writing – review & editing, Writing – original draft, Supervision, Resources, Project administration, Methodology, Funding acquisition, Conceptualization. **Guangda Wu:** Writing – review & editing, Writing – original draft, Validation, Methodology, Formal analysis, Data curation. **Xuefei Fu:** Resources, Project administration, Investigation, Conceptualization. **Xinyang Wang:** Writing – original draft, Resources, Methodology, Investigation.

Declaration of Competing Interest

The authors declare that they have no known competing financial interests or personal relationships that could have appeared to influence the work reported in this paper.

Data availability

Data will be made available on request.

Acknowledgement

The authors would like to gratefully acknowledge the financial support from National Key R&D Program of China (Grant No. 2020YFA0405700). Q. P. would like to acknowledge the support provided by National Natural Science Foundation of China (Grant No. 12272378), High-level Innovation Research Institute Program of Guangdong Province (Grant No. 2020B0909010003), and LiYing Program of the Institute of Mechanics, Chinese Academy of Sciences (Grant No. E1Z1011001).

References

[1] J. Yeh, S. Chang, Y. Hong, S. Chen, S. Lin, Anomalous decrease in X-ray diffraction intensities of Cu–Ni–Al–Co–Cr–Fe–Si alloy systems with multi-principal elements, Mater. Chem. Phys 103 (2007) 41.
[2] M. Chuang, M. Tsai, W. Wang, S. Lin, J. Yeh, Microstructure and wear behavior of AlxCo1.5CrFeNi1.5Tiy high-entropy alloys, Acta Mater 59 (2011) 6308.
[3] P. Zhang, Z. Xu, Z. Yao, Y. Liu, S. Lin, M. He, S. Lu, X. Wu, A high-corrosion-resistant high-entropy alloys (HEAs) coatings with single BCC solid solution structure by laser remelting, Mater. Lett. 324 (2022) 132728.
[4] Y. Li, J. Zhang, X. Huang, J. Liu, L. Deng, P. Han, Influence of laser power on microstructure evolution and properties of laser cladded FeNiCoCrMo HEA coatings, Mater. Today Commun. 35 (2023) 105615.
[5] F.Y. Shu, L. Wu, H.Y. Zhao, S.H. Sui, L. Zhou, J. Zhang, W.X. He, P. He, B.S. Xu, Microstructure and high-temperature wear mechanism of laser cladded CoCrBFeNiSi high-entropy alloy amorphous coating, Mater. Lett. 211 (2018) 235.
[6] C. Huang, Y. Zhang, R. Vilar, J. Shen, Dry sliding wear behavior of laser clad TiVCrAlSi high entropy alloy coatings on Ti–6Al–4V substrate, Mater. Des. 41 (2012) 338.
[7] Q. Ye, K. Feng, Z. Li, F. Lu, R. Li, J. Huang, Y. Wu, Microstructure and corrosion properties of CrMnFeCoNi high entropy alloy coating, Appl. Surf. Sci 396 (2017) 1420.
[8] G.J. Zhang, Q.W. Tian, K.X. Yin, S.Q. Niu, M.H. Wu, W.W. Wang, Y.N. Wang, J. C. Huang, Effect of Fe on microstructure and properties of AlCoCrFexNi (x=1.5, 2.5) high entropy alloy coatings prepared by laser cladding, Intermetallics 119 (2020) 106722.
[9] X.W. Qiu, Y.P. Zhang, C.G. Liu, Effect of Ti content on structure and properties of Al2CrFeNiCoCuTix high-entropy alloy coatings, J. Alloy Compd. 585 (2014) 282.
[10] Y. Guo, C. Li, M. Zeng, J. Wang, P. Deng, Y. Wang, In-situ TiC reinforced CoCrCuFeNiSi0.2 high-entropy alloy coatings designed for enhanced wear performance by laser cladding, Mater. Chem. Phys. 242 (2020) 122522.
[11] B.J. Alder, T.E. Wainwright, Phase transition for a hard sphere system, J. Chem. Phys. 27 (1957) 1208.
[12] L. Xie, G.D. Wu, Q. Peng, W.R. Wang, Molecular dynamics simulation on the dissolution and diffusion characteristics of FeCrAl alloy in liquid LBE, Ann. Nucl. Energy 192 (2023) 109983.
[13] S. Liu, L. Xie, Q. Peng, R. Li, Carbon nanotubes enhance the radiation resistance of bcc iron revealed by atomistic study, Materials 12 (2019) 217.
[14] Z. Sun, J. Zhang, H. Wang, G. Pan, T. Wang, L. Xie, Q. Peng, Defect, temperature, and strain effects on lattice heat conductivity of egg-tray graphene, Model. Simul. Mater. Sc 29 (2021) 45003.
[15] L. Xie, T. Sun, C. He, H. An, Q. Qin, Q. Peng, Effect of Angle, Temperature and Vacancy Defects on Mechanical Properties of PSI-Graphene, Crystals 9 (2019) 238.
[16] C. He, G. Pan, L. Xie, Q. Peng, Enhancement of Diffusion Assisted Bonding of the Bimetal Composite of Austenitic/Ferric Steels via Intrinsic Interlayers, Materials 14 (2021) 2416.
[17] L. Xie, T. Sun, C. He, J. Deng, H. Yi, X. Yang, Q. Qin, Q. Peng, Enhancement of toughness of SiC through compositing SiC-Al interpenetrating phase composites, Nanotechnology 31 (2020) 135706.
[18] Y. Chen, S. Wang, L. Xie, P. Zhu, R. Li, Q. Peng, Grain size and hydroxyl-coverage dependent tribology of polycrystalline graphene, Nanotechnology 30 (2019) 385701.
[19] Q. Qin, X. Liu, H. Wang, T. Sun, F. Chu, L. Xie, P. Brault, Q. Peng, Highly efficient desalination performance of carbon honeycomb based reverse osmosis membranes unveiled by molecular dynamics simulations, Nanotechnology 32 (2021).
[20] L. Xie, H. An, C. He, Q. Qin, Q. Peng, Mechanical properties of vacancy tuned carbon honeycomb, Nanomaterials-BASEL 9 (2019) 156.
[21] Z.H. Sun, J. Zhang, G.X. Xin, L. Xie, L.C. Yang, Q. Peng, Tensile mechanical properties of CoCrFeNiTiAl high entropy alloy via molecular dynamics simulations, Intermetallics 142 (2022) 107444.
[22] Q. Peng, F. Meng, Y. Yang, C. Lu, H. Deng, L. Wang, S. De, F. Gao, Shockwave generates < 100 > dislocation loops in bcc iron, Nat. Commun. (2018) 9.
[23] J. Li, Q. Fang, B. Liu, Y. Liu, Y. Liu, Mechanical behaviors of AlCrFeCuNi high-entropy alloys under uniaxial tension via molecular dynamics simulation, RSC Adv. (2016).
[24] Y. Zhang, H. Liu, J. Mo, M. Wang, Z. Chen, Y. He, W. Yang, C. Tang, Atomic-level crystallization in selective laser melting fabricated Zr-based metallic glasses, Phys. Chem. Chem. Phys. 21 (2019) 12406.
[25] S. Kurian, R. Mirzaeifar, Selective laser melting of aluminum nano-powder particles, a molecular dynamics study, Addit. Manuf. 35 (2020) 101272.
[26] H. Chen, Q. Fang, K. Zhou, Y. Liu, J. Li, Unraveling atomic-scale crystallization and microstructural evolution of a selective laser melted FeCrNi medium-entropy alloy, Crystengcomm (2020).
[27] T. Shun, L. Chang, M. Shiu, Microstructures and mechanical properties of multiprincipal component CoCrFeNiTix alloys, Mater. Sci. Eng.: A 556 (2012) 170.
[28] S. Gao, T. Kong, M. Zhang, X. Chen, Y.W. Sui, Y.J. Ren, J.Q. Qi, F.X. Wei, Y.Z. He, Q.K. Meng, Z. Sun, Effects of titanium addition on microstructure and mechanical properties of CrFeNiTix (x = 0.2–0.6) compositionally complex alloys, J. Mater. Res. 34 (2019) 819.
[29] M.S. Daw, S.M. Foiles, M.I. Baskes, The embedded-atom method: a review of theory and applications, Mater. Sci. Rep. 9 (1993) 251.
[30] X.W. Zhou, R.A. Johnson, H.N.G. Wadley, Misfit-energy-increasing dislocations in vapor-deposited CoFe/NiFe multilayers, Phys. Rev. B 69 (2004) 144113.
[31] J. Liu, Molecular dynamic study of temperature dependence of mechanical properties and plastic inception of CoCrCuFeNi high-entropy alloy, Phys. Lett. A 384 (2020) 126516.
[32] H. Liu, C. Peng, X. Li, S. Wang, L. Wang, The Effect of Phase Separation on the Mechanical Behavior of the Co–Cr–Cu–Fe–Ni High-Entropy Alloy, Materials 14 (2021) 6523.
[33] M. Wang, S. Guo, X. Lin, W.D. Huang, Research on the nucleation and growth of high-entropy alloy, Mater. Lett. 285 (2021) 129206.
[34] M. Imafuku, Y. Sasajima, R. Yamamoto, M. Doyama, Computer simulations of the structures of the metallic superlattices Au/Ni and Cu/Ni and their elastic moduli, J. Phys. F., Met. Phys. 16 (1986) 823.
[35] L. Xie, P. Brault, A. Thomann, J. Bauchire, AlCoCrCuFeNi high entropy alloy cluster growth and annealing on silicon: A classical molecular dynamics simulation study, Appl. Surf. Sci. 285 (2013) 810.
[36] S. Plimpton, Fast parallel algorithms for short-range molecular dynamics, J. Comput. Phys. 117 (1) (1995).
[37] A. Stukowski, Visualization and analysis of atomistic simulation data with OVITO–the Open Visualization Tool, Model. Simul. Mater. SC 18 (2010) 15012.
[38] D. Faken, H. Jónsson, Systematic analysis of local atomic structure combined with 3D computer graphics, Comp. Mater. Sci. 2 (1994) 279.
[39] L. Xie, P. Brault, A. Thomann, X. Yang, Y. Zhang, G. Shang, Molecular dynamics simulation of Al–Co–Cr–Cu–Fe–Ni high entropy alloy thin film growth, Intermetallics 68 (2016) 78.
[40] R. Li, T. Liu, X. Chen, S. Chen, Y. Fu, L. Liu, Influence of interface structure on nanoindentation behavior of Cu/Ni multilayer film: Atomic scale simulation, Acta Phys. Sin-ch. Ed 67 (2018) 190202.
[41] Z. Sun, B. Liu, C. He, L. Xie, Q. Peng, Shift of Creep Mechanism in Nanocrystalline NiAl Alloy, Materials 12 (2019) 2508.
[42] Q. Qin, W. He, L. Xie, J. Deng, X. Zhu, Q. Peng, Nonlinear diffusion, bonding, and mechanics of the interface between austenitic steel and iron, Phys. Chem. Chem. Phys. 21 (2019) 1464.
[43] L. Xie, H. An, Q. Peng, Q. Qin, Y. Zhang, Sensitive Five-Fold Local Symmetry to Kinetic Energy of Depositing Atoms in Cu-Zr Thin Film Growth, Materials 11 (2018) 2548.
[44] H. Tatsumi, C.R. Kao, H. Nishikawa, Solid-state bonding behavior between surface-nanostructured Cu and Au: a molecular dynamics simulation, Sci. Rep.-UK 12 (2022).
[45] Y. Wang, S. Ma, X. Chen, J. Shi, Y. Zhang, J. Qiao, Optimizing mechanical properties of AlCoCrFeNiTi x high-entropy alloys by tailoring microstructures, Acta Metall. Sin. (Engl. Lett.) 26 (2013) 277.
[46] Z. Pei, S. Zhang, Y. Lei, F. Zhang, M. Chen, Decoupling between Shockley partials and stacking faults strengthens multiprincipal element alloys, Proc. Natl. Acad. Sci. 118 (2021).
[47] B. Wu, J. Man, G. Duan, L. Zhang, X. Du, Y. Liu, C. Esling, Constructing a heterogeneous microstructure in the CoCrFeNi-based high entropy alloy to obtain a superior strength-ductility synergy, Mater. Sci. Eng.: A 886 (2023) 145669.
[48] L. Qiao, R.V. Ramanujan, J. Zhu, Tensile deformation behavior and strengthening mechanism of aFe2.5Ni2.5CrAl multi-principal element alloy, Mater. Des. 230 (2023) 111963.
[49] X. Gao, R. Chen, T. Liu, H. Fang, G. Qin, Y. Su, J. Guo, High-entropy alloys: a review of mechanical properties and deformation mechanisms at cryogenic temperatures, J. Mater. Sci. 57 (2022) 6573.